Soft Matter

Accepted Manuscript

This article can be cited before page numbers have been issued, to do this please use: J. A. Sanz-Herrera, J. Barrasa Fano, M. Cóndor and H. Van Oosterwyck, *Soft Matter*, 2020, DOI: 10.1039/D0SM00789G.

ROYAL SOCIETY OF CHEMISTRY

rsc.li/soft-matter-journal

View Article Online
DOI: 10.1039/D0SM00789G

Soft Matter

ARTICLE TYPE

Cite this: DOI: 00.0000/xxxxxxxxxx

Inverse method based on 3D nonlinear physically constrained minimisation in the framework of traction force microscopy

J.A. Sanz-Herrera,[a] J. Barrasa-Fano,[b] M. Cóndor,[b] and H. Van Oosterwyck*[b,c]

Received Date
Accepted Date

DOI: 00.0000/xxxxxxxxxx

Traction force microscopy is a methodology that enables to estimate cellular forces from the measurement of the displacement field of an extracellular matrix (ECM)–mimicking hydrogel that a cell is mechanically interacting with. In this paper, a new inverse and physically-consistent methodology is developed and implemented in the context of 3D nonlinear elasticity. The proposed method searches for a displacement field that approximates the measured one, through the imposition of fulfillment of equilibrium with real and known forces acting in the hydrogel. The overall mathematical formulation leads to a constrained optimisation problem that is treated through a Lagrange operator and that is solved numerically by means of a nonlinear finite element framework. In order to illustrate the potential and enhanced accuracy of the proposed inverse method, it is applied to a total of 5 different real cases of cells cultured in a 3D hydrogel that is considered to behave as a nonlinear elastic material. Different error indicators are defined in order to compare ground truth simulated displacements and tractions to the ones recovered by the new inverse as well as by the forward method. Results indicate that the evaluation of displacement gradients leads to errors, in terms of recovered tractions, that are more than three times lower (on average) for the inverse method compared to the forward method. They highlight the enhanced accuracy of the developed methodology and the importance of appropriate inverse methods that impose physical constraints to traction and stress recovery in the context of traction force microscopy.

1 Introduction

The importance of mechanical factors in cell biology and physiology has been evidenced in many publications in the last decades[1–6]. Given this importance, the measurement and quantification of mechanical variables in cell biological environments is essential in order to develop hypotheses and theories which eventually may explain a certain observed behavior.

Traction force microscopy (TFM) allows to estimate the forces exerted by a cell in contact with a substrate that mimics its extracellular matrix (ECM). These forces are inferred from the measurement of the deformation of the substrate, provided the mechanical properties of the substrate are known. Typically, the deformational state of the substrate is determined from the motion of marker points from a deformed (stressed) to an undeformed (relaxed) configuration. TFM has been applied to investigate force exertion during cell migration on flat (2D) substrates[7–11], as well as in 3D matrices[12–15]. The reader is referred to fig. 1 where a scheme of the overall methodology is sketched for a cell embedded in a 3D hydrogel.

Even though a TFM approach is simplistic from a conceptual point of view, it introduces important technical, theoretical, computational and numerical challenges, especially for cells embedded in 3D matrices. Following the elasticity theory (either linear or nonlinear), from a given displacement field (assumed as true) as an input data, the solution of the remaining variables, i.e. strain, stress and tractions, turns into an algebraic problem, which involves only the derivatives of the displacement field following the compatibility and material constitutive equations, as well as the relation between the outward surface normal and the stress tensor, i.e. Cauchy's formula. Therefore, the problem can be straightforwardly solved following a so-called *forward method*. Since the displacement field is obtained from measurements at discrete locations, the problem only concerns the numerical treatment of the derivative kernel. Finite differences are employed[13], as well as in conjunction with an improved noise filtering technique[16,17]. Base interpolation (shape) functions can be used as well under a Finite Element Method (FEM) scheme as an alternative to solve the problem[18,19]. In the case of well-characterized materials such that any deviation from a certain constitutive law

[a] *Escuela Técnica Superior de Ingeniería, Universidad de Sevilla, Seville, Spain.*
[b] *Biomechanics section, Department of Mechanical Engineering, KU Leuven, Leuven, Belgium. E-mail: hans.vanoosterwyck@kuleuven.be*
[c] *Prometheus division of Skeletal Tissue Engineering, KU Leuven, Leuven, Belgium.*

View Article Online
DOI: 10.1039/D0SM00789G

is negligible, this kind of direct approaches do not assure the fulfillment of equilibrium of internal forces with real and known acting forces, as far as the obtained displacement field is not error–free despite any filtering techniques.

The formulation of the problem including force equilibrium following an *inverse method* leads to an incompatible displacement solution versus the measured (noisy) displacements, as well as unstable traction computation[20], rendering the problem ill-posed. In this context, a regularization process is followed to avoid overfitting such as L_2 (Tikhonov) regularization:

$$\min_{\mathbf{t}} \left(||\mathbf{G}\mathbf{t} - \mathbf{u}||_2^2 + \lambda ||\mathbf{t}||_2^2 \right) \quad (1)$$

where $\mathbf{u}$ is the recovered input displacement field, $\mathbf{t}$ the cell boundary tractions and $\mathbf{G}$ the compliance matrix of the (discretized) algebraic (linearized) system. The first term of the objective function in (1) expresses equilibrium of forces, while the second term is the regularization term that in this case promotes traction solutions with smaller norm. The parameter λ is the so-called regularization parameter which needs to be chosen *a priori* under some mathematical[21] or empirical[22] criteria. This kind of approaches has been implemented by means of a BEM, FEM or Fourier transformation techniques (the reader is referred to Ref.[20] for a review of the methods).

An alternative formulation of Eq. (1) has been presented in Ref.[23]. In this paper, the author considered the linear elasticity equations as a constraint on a regularization procedure similar to (1). Results are presented for different cells on linear elastic 2D substrates[23,24]. While the method was initially developed for planar substrates, it was later extended to a cell embedded in a 3D substrate for a cell geometry that was simplified to an ellipsoid[25]. As cells are typically not ellipsoidal, the applicability of the method towards real experimental conditions may be somewhat limited. Moreover, the method has not been applied to nonlinear elastic substrates, which is typically the case for natural ECM-derived substrates, like collagen and fibrin[14].

In this paper we formulate and numerically implement a new physics-based nonlinear inverse method (PBNIM) in the framework of TFM. Physics-based refers to the fact that the fulfillment of equilibrium of internal forces with real and known acting forces as a universal physical law is imposed as a constraint to the solution of the displacement field. Novelty of the paper relates to the formulation of the inverse problem, as well as the numerical implementation and solution of the problem, which is fully 3D and considers nonlinear ECM mechanics, including finite strains and hyperelasticity. As previously said, the minimisation problem includes the imposition of physical constraints, in particular equilibrium of forces in the ECM, through a Lagrange operator similarly to recent constrained problems in the context of data driven techniques[26]. The optimal solution of the overall minimisation problem is analytically derived which avoids the implementation of costly solvers based on searching algorithms. Moreover, the resulting optimal solution is nonlinear due to the assumed nonlinear elastic behavior of the ECM-mimicking hydrogel and considered finite strains, which is implemented following a Newton-Raphson iterative scheme. The numerical treatment of the problem is elaborated in detail in the present paper by means of the FEM. The method is applied to the geometry of a total of 5 real cells embedded in a 3D nonlinear matrix. Several statistics–based error indicators are defined in order to quantify the performance of the new inverse and the forward method versus a ground truth reference solution. While displacement fields are well recovered by both methods, errors in the recovered tractions are more than three times lower (on average) in the case of the inverse approach.

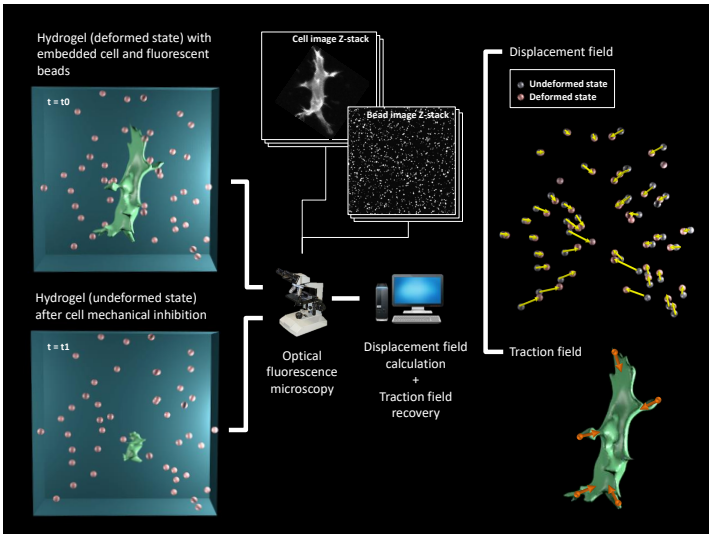

Fig. 1 TFM workflow. Cells are seeded in an ECM-mimicking hydrogel with embedded fluorescent beads. A first set (z-stack) of microscopy images of the fluorescent beads are acquired while cells are applying forces to the hydrogel (deformed state at $t = t_0$). Images of the cells can also be acquired to locate the cell boundary. Next, cell mechanical interactions are inhibited and a second set of microscopy images is acquired (undeformed state at $t = t_1$). Finally, the two image data sets of the fluorescent beads are used to calculate the displacement field of the hydrogel. This displacement field is then combined with a model of the hydrogel's mechanical behavior to recover cellular forces.

2 Mechanical problem underlying TFM

The mechanical problem underlying TFM is sketched in fig. 2a. A cell exerts forces on its surrounding ECM through its internal cytoskeletal (CSK) machinery and its focal adhesions (FA) that connects the cell to the ECM[27]. As explained above, positional information in stressed and relaxed configurations are available at sampling points (discrete locations) in the hydrogel domain (fig. 2a). From that information, the reconstruction of the displacement field and the remaining mechanical variables are explained next.

Displacement field recovery

Different time point images of the deformed (stressed) and final undeformed (relaxed) configurations of the hydrogel region are the input data at this point, hydrogel is assumed to be an elastic (conservative) material such that any dissipative energy source is neglected. Voxelized 3D data are converted into a displacement field following any of the methods found in literature such as Particle Image Velocimetry (PIV)[28,29], Particle Tracking Velocimetry

View Article Online
DOI: 10.1039/D0SM00789G

(PTV) [12,30] or Free Form Deformation (FFD)–based non-rigid image registration [31]. Briefly, PTV maps individual beads motions such that the displacement field is available at those (discrete) locations. On the other hand, PIV follows digital image correlation techniques and the mapping of tracked beads is established over regular (voxel) blocks. FFD, uses a deformable mesh controlled by B-spline based functions which avoids individual particle tracking and retrieves a continuous displacement field. The details of the FFD method as well as its advantages versus PTV and PIV methods have been shown in Jorge-Peñas et al. [31].

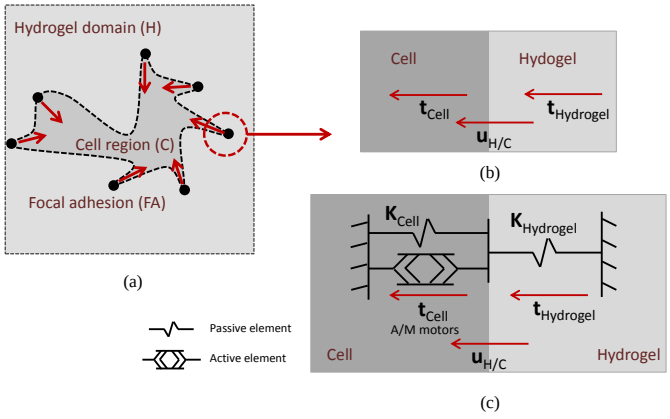

Fig. 2 Mechanical problem underlying TFM. (a) Sketch of a cell embedded in a hydrogel. (b) Scheme of cellular forces at cell-hydrogel interface region. (c) Simplified 1D linear model of (b) accounting for passive and active cytoskeletal (CSK) machinery of the cell.

Traction analysis

From a given displacement field $\mathbf{u}_H$ (subscript H referring to hydrogel domain), at discrete locations of the domain of the hydrogel, tractions at the boundary of the cell are estimated according to the forward or inverse methodologies. In this paper, the forward method is briefly introduced next in the framework of the FEM, and a new version of the inverse method is developed in the next sections.

From the recovered displacement field at this location $\mathbf{u}_{H/C}$ at the cell boundary (with subscript H/C referring to hydrogel/cell interface), tractions may be estimated in a first simplified approach according to a 1D linear model of cell-ECM mechanical interactions (fig. 2). We assume that displacements at the boundary $\mathbf{u}_{H/C}$ are affine. The CSK of the cell may be simply modeled by means of active and passive elements that act in parallel. Active elements account for actin filaments and myosin motors whereas the passive elements represent the overall stiffness of the CSK as a passive material (the reader is referred to Refs. [27,32,33] for a discussion on this kind of CSK models). The hydrogel is represented as a passive material in this simplified model. Equilibrium of forces in this model yields,

$$\mathbf{t}_{Cell} = \mathbf{t}_{Hydrogel} \tag{2}$$

Using the split of cell tractions into its active and passive components,

$$\mathbf{t}_{C-act} + \mathbf{t}_{C-pass} = \mathbf{t}_{Hydrogel} \tag{3}$$

When using a linear relationship (without loss of generality) between displacements and tractions, we obtain,

$$\mathbf{t}_{C-act} + \mathbf{K}_{C-pass} \cdot \mathbf{u}_{H/C} = \mathbf{K}_{Hydrogel} \cdot \mathbf{u}_{H/C} \tag{4}$$

Therefore, this simplified 1D linear model allows to draw the following conclusions which are applicable to the more general case of 3D TFM:

1. TFM allows to estimate total cell tractions $\mathbf{t}_{Cell}$ through the displacement field available at the cell-hydrogel boundary $\mathbf{u}_{H/C}$.
2. Discrimination between active or passive tractions is not possible unless a reliable estimation of the passive stiffness of the CSK is available.
3. Under the assumption that passive tractions are negligible, active tractions exerted by the cell CSK machinery may be estimated through $\mathbf{u}_{H/C}$ following Eq. (4).
4. Total cell tractions $\mathbf{t}_{Cell}$, or active tractions $\mathbf{t}_{C-act}$ under the assumption 3, are only a function of the recovered displacement field $\mathbf{u}_{H/C}$ and the mechanical properties of the hydrogel domain (represented through $\mathbf{K}_{Hydrogel}$ in the simplified 1D linear model). Therefore, the main sources of error are due to the methods related to the estimation of the displacement field, and the measurement of the mechanical properties of the hydrogel.

3 Traction recovery by means of the forward method

The forward method, as well as the inverse method introduced in the next section, is developed in the framework of finite strain hyperelasticity. The forward displacement solution is assumed to be the recovered (measured) displacement field in the hydrogel domain. Therefore, given the recovered displacement field $\mathbf{u}_i$ at discrete points i refering to the spatial (Eulerian) description*, the motion of a material point $\mathbf{X}_i$ is given by,

$$\mathbf{X}_i = \mathbf{x}_i - \mathbf{u}_i \tag{5}$$

The deformation gradient is defined as,

$$\mathbf{F} = \frac{\partial \mathbf{x}}{\partial \mathbf{X}} \tag{6}$$

Using (5) in (6) yields,

$$\mathbf{F}^{-1} = \mathbf{I} - \frac{\partial \mathbf{u}}{\partial \mathbf{x}} \tag{7}$$

$\mathbf{I}$ being the identity matrix in Eq (7). The derivative of the second term on the right hand side of Eq. (7) may be obtained by means

* Remark that the reference configuration in TFM is the deformed hydrogel and stressed cell state after which a relaxed hydrogel configuration is achieved (see section 2).

View Article Online
DOI: 10.1039/D0SM00789G

of a general numerical procedure, such as finite differences or specific interpolating functions[13,16,17]. Note that in this case, a consistent numerical method such as finite or boundary elements is not necessary to account for the (discrete) deformation gradient and subsequent stress and tractions quantities as is developed next. Nonetheless, the FEM is used in this paper as the numerical solver both for the forward and inverse methodologies. Then, the displacement field is approached as follows:

$$\mathbf{u} \approx \mathbf{N}(\mathbf{x}) \cdot \mathbf{u}_i \quad \text{and} \quad \frac{\partial \mathbf{u}}{\partial \mathbf{x}} \approx \frac{\partial \mathbf{N}}{\partial \mathbf{x}} \cdot \mathbf{u}_i \tag{8}$$

with the displacement field $\mathbf{u}_i$ in (8) defined at nodal locations i. $\mathbf{N}(\mathbf{x})$ is the matrix which contains standard shape functions associated to element interpolation. Then, using (8) in (7), the gradient of displacements and the discretized inverse of the deformation gradient is computed at the Gauss points $\mathbf{x}_j$ of the finite element mesh†,

$$\mathbf{F}_j^{-1} \approx \mathbf{I} - \left.\frac{\partial \mathbf{N}}{\partial \mathbf{x}}\right|_{\mathbf{x}=\mathbf{x}_j} \cdot \mathbf{u}_i \tag{9}$$

The right Cauchy-Green tensor is defined as,

$$\mathbf{C} = \mathbf{F}^T \cdot \mathbf{F} \tag{10}$$

Moreover, the Cauchy (true) stresses can be obtained through the following expression[34],

$$\sigma = \frac{2}{J}\mathbf{F} \cdot \frac{\partial \psi}{\partial \mathbf{C}} \cdot \mathbf{F}^T \tag{11}$$

where $J = \det(\mathbf{F})$ and ψ is the strain energy function of the material (hydrogel). Eq. (11) can be further developed for isotropic materials as follows (see Ref.[34]),

$$\sigma = \frac{2}{J}\mathbf{F}\left[\left(\frac{\partial \psi}{\partial I_1} + I_1 \frac{\partial \psi}{\partial I_2}\right)\mathbf{I} - \frac{\partial \psi}{\partial I_2}\mathbf{C} + I_3 \frac{\partial \psi}{\partial I_3}\mathbf{C}^{-1}\right] \cdot \mathbf{F}^T \tag{12}$$

For the sake of simplicity, a quasi-incompressible Neo-Hookean behavior is selected to describe the hydrogel mechanics. Hence,

$$\psi = \frac{G}{2}(\bar{I}_1 - 3) + \frac{\kappa}{2}(J-1)^2 \quad \text{and} \quad \bar{I}_1 = J^{-2/3} I_1 \tag{13}$$

where G and κ are the shear and bulk moduli of the material, respectively. I_1 is the first invariant (trace) of $\mathbf{C}$, and $\bar{I}_1$ is the first invariant of its isochoric part.

Using (13) in (12), and after some algebraic manipulations, yields,

$$\sigma = \mathbf{F}\left[GJ^{-5/3} \cdot \mathbf{I} + \left[\kappa(J-1) - \frac{G}{3J}\bar{I}_1\right] \cdot \mathbf{C}^{-1}\right] \cdot \mathbf{F}^T \tag{14}$$

Note that the right hand side of (14) can be expressed as a function of the deformation gradient according to the definitions given above. Moreover, the deformation gradient is obtained at discrete Gauss points $\mathbf{x}_j$ of the mesh according to Eq. (9) as a function of a (given) displacement field and (chosen) interpolation functions. In a FEM framework (as followed in this paper) these interpolation functions are well described, however, other interpolation techniques may be used including B-Splines[31,35], or finite differences[13,17]. Hence, Cauchy stresses σ_j can be computed at those Gauss points as well. Finally, tractions are computed following Cauchy's formula as,

$$\mathbf{t}_i^n = \sigma_i \cdot \mathbf{n}_i \tag{15}$$

$\mathbf{t}_i^n$ is the traction vector associated to the spatial configuration at nodal points i of the finite element mesh. σ_i is the Cauchy stress tensor at nodal points i after an averaging procedure of σ_j from Gauss points is conducted[36]. Finally, $\mathbf{n}_i$ is the outward normal to node i. The normal is numerically computed at nodal points from the surfaces of elements of the finite element mesh in the deformed (reference) configuration.

4 Traction recovery by means of a physics-based nonlinear inverse method (PBNIM)

According to the discussion in section 2, the displacement field is given in the hydrogel domain. Moreover, given certain assumptions (see also section 2), cell boundary tractions can be estimated as a function of the displacement field in the hydrogel domain. Therefore, our domain of analysis is restricted to the hydrogel interior domain $\Omega_H(\mathbf{x})$ and cell boundary $\Gamma_{H/C}(\mathbf{x})$, see fig. 2a.

The proposed PBNIM includes two main ingredients: (i) Search for an inverse displacement field solution $\mathbf{u}$ that is as close as possible to the recovered (measured) field $\mathbf{u}^\star$, and (ii) which fulfills equilibrium of internal forces with real and known forces acting in the hydrogel domain region. This statement can be seen as a minimization problem including the equilibrium constraint equation, and can be mathematically described as follows:

$$\begin{array}{c} \min_{\mathbf{u}} \ \left(\frac{1}{2}||\mathbf{u}-\mathbf{u}^\star||_2^2 \right) \\ s.t. \\ \Theta = 0 \end{array} \tag{16}$$

where Θ generically represents the equilibrium – i.e. the physical– constraint manifold where the desired displacement solution $\mathbf{u}$ must lie. The functional Θ is selected in terms of the Principle of Virtual Work (PVW) equation for convenience in its subsequent finite element numerical discretization as presented in section 5. The continuum and scalar PVW equation is developed in this section. Geometrically, the problem can be seen as the projection of $\mathbf{u}^\star$ over the manifold Θ.

The equilibrium constraint equation Θ can be enforced in (16) by means of a (continuum and scalar) Lagrange multiplier operator η as follows,

$$\min_{\mathbf{u}} \left(\frac{1}{2}||\mathbf{u}-\mathbf{u}^\star||_2^2 + \Theta \cdot \eta \right) \tag{17}$$

Remark that the equilibrium constraint term in Eq. (17) can be interpreted as a regularization term according to Eq. (1). Using the Gateaux derivative, Eq. (17) has its minimum (analytical)

† The finite element mesh in TFM is derived from the deformed hydrogel state.

View Article Online
DOI: 10.1039/D0SM00789G

stationary solution at,

$$\delta\mathbf{u}=\mathbf{0} \;\rightarrow\; \mathbf{u}+\frac{\delta\Theta}{\delta\mathbf{u}}\cdot\eta=\mathbf{u}^{\star} \tag{18a}$$

$$\delta\eta=0 \;\rightarrow\; \Theta=0 \tag{18b}$$

As previously discussed, the equilibrium constraint equation Θ is proposed to be defined in terms of the principle of virtual work. In fact, the PVW is intrinsically defined as an equilibrium equation such that its fulfillment ensures the equilibrium of internal (stress) forces with real and known acting external forces[34]. Hence,

$$\Theta := \delta W(\mathbf{u},\delta\mathbf{u}) \tag{19}$$

with $\delta\mathbf{u}$ being a kinematically admissible (virtual) displacement field. Since the software Simulia Abaqus is used in the numerical implementation (see next section), the updated Lagrangian version of the PVW is selected. Therefore, in the absence of body forces, the PVW yields,

$$\delta W(\mathbf{u},\delta\mathbf{u})=\int_{\Omega}\tau:\delta\varepsilon dv-\int_{\Gamma}\mathbf{t}\cdot\delta\mathbf{u}ds=0 \tag{20}$$

with, τ being the Kirchhoff stress tensor, $\tau=J\sigma$, and,

$$\delta\varepsilon=\frac{1}{2}(\nabla\delta\mathbf{u}+\nabla^{T}\delta\mathbf{u}) \tag{21}$$

Substitution of Eq. (19) in Eqs. (18a)–(18b), and using the definition of the PVW in (20), yields the following set of nonlinear equations:

$$\mathbf{u}+D\delta W(\mathbf{u},\delta\mathbf{u})\cdot\eta=\mathbf{u}^{\star} \tag{22a}$$

$$\delta W(\mathbf{u},\delta\mathbf{u})=\int_{\Omega}\tau:\delta\varepsilon dv-\int_{\Gamma}\mathbf{t}\cdot\delta\mathbf{u}ds=0 \tag{22b}$$

Next, a linearization procedure of Eq. (22b) is followed by means of a (first order) Taylor expansion around a configuration $\mathbf{u}$,

$$\delta W(\mathbf{u},\delta\mathbf{u})+D\delta W(\mathbf{u},\delta\mathbf{u})[\Delta\mathbf{u}]=0 \tag{23}$$

Therefore, the linearized set of equations of the proposed inverse method yields,

$$\mathbf{u}+D\delta W(\mathbf{u},\delta\mathbf{u})\cdot\eta=\mathbf{u}^{\star} \tag{24a}$$

$$\delta W(\mathbf{u},\delta\mathbf{u})+D\delta W(\mathbf{u},\delta\mathbf{u})[\Delta\mathbf{u}]=0 \tag{24b}$$

The directional derivative term $D\delta W(\mathbf{u},\delta\mathbf{u})[\Delta\mathbf{u}]$ is split into internal and external work components,

$$D\delta W(\mathbf{u},\delta\mathbf{u})[\Delta\mathbf{u}]=D\delta W_{\text{int}}(\mathbf{u},\delta\mathbf{u})[\Delta\mathbf{u}]-D\delta W_{\text{ext}}(\mathbf{u},\delta\mathbf{u})[\Delta\mathbf{u}] \tag{25}$$

with

$$D\delta W_{\text{int}}(\mathbf{u},\delta\mathbf{u})[\Delta\mathbf{u}]=\int_{\Omega}D(\tau:\delta\varepsilon)[\Delta\mathbf{u}]dv \tag{26}$$

$$D\delta W_{\text{ext}}(\mathbf{u},\delta\mathbf{u})[\Delta\mathbf{u}]=\int_{\Gamma}D(\mathbf{t}\cdot\delta\mathbf{u})[\Delta\mathbf{u}]ds \tag{27}$$

The internal work term (26) is developed through the Jaumann (corotational) derivative of the Kirchhoff stres tensor as follows[37],

$$D\delta W_{\text{int}}(\mathbf{u},\delta\mathbf{u})[\Delta\mathbf{u}]=\int_{\Omega}\nabla\delta\mathbf{u}:(J\mathbb{c}+\mathbb{H}):\nabla\Delta\mathbf{u}dv+\int_{\Omega}\tau:[(\nabla\delta\mathbf{u})^{T}\nabla\Delta\mathbf{u}]dv \tag{28}$$

where

$$\varepsilon=\frac{1}{2}(\nabla\Delta\mathbf{u}+\nabla^{T}\Delta\mathbf{u}) \tag{29}$$

with $\mathbb{c}$ the spatial elasticity tensor and defined (in index notation) as,

$$c_{ijkl}=\frac{1}{J}F_{iI}F_{jJ}F_{kK}F_{lL}C_{IJKL} \tag{30}$$

and,

$$H_{ijkl}=\frac{1}{2}\left(\delta_{jk}\tau_{il}+\delta_{ik}\tau_{jl}+\delta_{jl}\tau_{ik}+\delta_{il}\tau_{jk}\right) \tag{31}$$

Note that repeated index denotes summation in (30). On the other hand, the material elasticity tensor is defined as follows,

$$\mathbb{C}=4\frac{\partial^{2}\psi}{\partial\mathbf{C}\partial\mathbf{C}} \tag{32}$$

The integration of the traction (surface) forces present in the right hand side of Eq. (27), is treated by means of a parametrization of the surface area. The reader is referred to Bonet and Wood[37] for additional details.

The numerical implementation of Eqs. (18a), (18b) and (23) is developed in the next section.

5 Numerical implementation

Linearized Eqs. (24) are discretized, in a FE framework, following two principal ingredients:

1. Discretization of field variables: Such that, $\Delta\mathbf{u}\approx\mathbf{N}^{(e)}\cdot\Delta\mathbf{u}^{i}$ and $\delta\mathbf{u}\approx\mathbf{N}^{(e)}\cdot\delta\mathbf{u}^{i}$. Where $\mathbf{N}^{(e)}$ is the matrix that contains the shape (interpolation) functions in element (e). On the other hand, $\Delta\mathbf{u}^{i}$, $\delta\mathbf{u}^{i}$, $\mathbf{u}^{\star,i}$ and η^{i} are vectors that contain the discrete values of $\Delta\mathbf{u}$, $\delta\mathbf{u}$, $\mathbf{u}^{\star}$ and η at node positions i.

2. Domain discretization into finite elements: Such that $\int_{\Omega}\bullet=\sum_{e=1}^{N_{el}}\int_{\Omega_{e}}\bullet$, where Ω_{e} is the finite element domain of element (e) and N_{el} the number of elements of the mesh.

View Article Online
DOI: 10.1039/D0SM00789G

Therefore, using the discretization before Eqs. (24) yield,

$$\mathbf{u}^i_{k+1} + \sum_{e=1}^{N_{el}} D\delta W^{(e)}(\mathbf{u}^i_k, \delta\mathbf{u}^i)\cdot\eta^i_{k+1} = \mathbf{u}^{\star,i} \tag{33a}$$

$$\sum_{e=1}^{N_{el}} \delta W^{(e)}(\mathbf{u}^i_k, \delta\mathbf{u}^i) + \sum_{e=1}^{N_{el}} D\delta W^{(e)}(\mathbf{u}^i_k, \delta\mathbf{u}^i)[\Delta\mathbf{u}^i] = \mathbf{0} \tag{33b}$$

where $\mathbf{u}^i_{k+1} = \mathbf{u}^i_k + \Delta\mathbf{u}^i$, with $\mathbf{u}^i_k$ the solution of the $k-th$ iteration of the Newton-Raphson procedure. The development of the field and domain discretization in (33), with the definitions introduced in section 4 and after some algebraic manipulations (the reader is referred to Refs.[37,38] for additional details of the implementation), yields the following system in matrix form:

$$\mathbf{u}^i_{k+1} + \mathbb{A}_{e=1}^{N_{el}}\, \mathbf{K}^{(e)}\cdot\eta^i_{k+1} = \mathbf{u}^{\star,i} \tag{34a}$$

$$\mathbb{A}_{e=1}^{N_{el}} \left(\mathbf{F}^{(e),\text{int}}_k - \mathbf{F}^{(e),\text{ext}}_k\right) + \mathbb{A}_{e=1}^{N_{el}}\, \mathbf{K}^{(e)}\cdot\Delta\mathbf{u}^i = \mathbf{0} \tag{34b}$$

where $\mathbb{A}$ is the finite element assembly operator, and $\mathbf{F}^{(e),\text{int}}_k$ and $\mathbf{F}^{(e),\text{ext}}_k$ the element vector (discretized version) of internal and external forces of Eq. (17) evaluated at the $k-th$ iteration. $\mathbf{K}^{(e)}$ is the tangent element matrix. After assembly, Eqs. (34) yield,

$$\mathbf{u}^i_{k+1} + \mathbf{K}\cdot\eta^i_{k+1} = \mathbf{u}^{\star,i} \tag{35a}$$

$$\mathbf{F}^{\text{int},i}_k - \mathbf{F}^{\text{ext},i}_k + \mathbf{K}\cdot\Delta\mathbf{u}^i = \mathbf{0} \tag{35b}$$

Eqs. (35) can be expressed in matrix form as follows,

$$\begin{bmatrix} \mathbf{I} & \mathbf{K} \\ \mathbf{K} & \mathbf{0} \end{bmatrix} \cdot \begin{bmatrix} \mathbf{u}^i_{k+1} \\ \eta^i_{k+1} \end{bmatrix} = \begin{bmatrix} \mathbf{u}^{\star,i} \\ \mathbf{F}^{\text{ext},i}_k - \mathbf{F}^{\text{int},i}_k - \mathbf{K}\cdot\mathbf{u}^i_k \end{bmatrix} \tag{36}$$

Eq. (36) accounts for all the degrees of freedom of the nodes of the FE discretization. Next, Eq. (36) is ordered according to cell boundary nodes H/C and hydrogel internal nodes H as follows,

$$\begin{bmatrix} \mathbf{I} & \mathbf{0} & \mathbf{K}(H,H) & \mathbf{K}(H,H/C) \\ \mathbf{0} & \mathbf{I} & \mathbf{K}(H/C,H) & \mathbf{K}(H/C,H/C) \\ \mathbf{K}(H,H) & \mathbf{K}(H,H/C) & \mathbf{0} & \mathbf{0} \\ \mathbf{K}(H/C,H) & \mathbf{K}(H/C,H/C) & \mathbf{0} & \mathbf{0} \end{bmatrix} \cdot \begin{bmatrix} \mathbf{u}^i_{k+1}(H) \\ \mathbf{u}^i_{k+1}(H/C) \\ \eta^i_{k+1}(H) \\ \eta^i_{k+1}(H/C) \end{bmatrix} = \begin{bmatrix} \mathbf{u}^{\star,i}(H) \\ \mathbf{u}^{\star,i}(H/C) \\ \mathbf{F}^{\text{ext},i}_k(H) - \mathbf{F}^{\text{int},i}_k(H) \\ \mathbf{F}^{\text{ext},i}_k(H/C) - \mathbf{F}^{\text{int},i}_k(H/C) \end{bmatrix} - \begin{bmatrix} \mathbf{0} \\ \mathbf{0} \\ \begin{bmatrix} \mathbf{K}(H,H) & \mathbf{K}(H,H/C) \\ \mathbf{K}(H/C,H) & \mathbf{K}(H/C,H/C) \end{bmatrix} \cdot \begin{bmatrix} \mathbf{u}^i_k(H) \\ \mathbf{u}^i_k(H/C) \end{bmatrix} \end{bmatrix} \tag{37}$$

$\mathbf{F}^{\text{ext},i}(H/C)$ in the fourth row of the right hand side of Eq. (37) represents the nodal reaction forces exerted by the cell at cell-hydrogel boundary nodes and is an unknown variable in the system above. Therefore, the associated Lagrange multiplier is prescribed as a boundary (Dirichlet) condition as $\eta^i(H/C) = \mathbf{0}$. Note that, in practical terms, this is equivalent to impose equilibrium of internal (stress) forces with real acting forces, assumed to be known only in the hydrogel interior. Indeed, nodal reaction forces at hydrogel internal nodes $\mathbf{F}^{\text{ext},i}(H)$ must be zero in the absence of any body or active forces in the passive hydrogel interior. Hence Eq. (37) can be rewritten as,

$$\begin{bmatrix} \mathbf{I} & \mathbf{0} & \mathbf{K}(H,H) \\ \mathbf{0} & \mathbf{I} & \mathbf{K}(H/C,H) \\ \mathbf{K}(H,H) & \mathbf{K}(H,H/C) & \mathbf{0} \end{bmatrix} \cdot \begin{bmatrix} \mathbf{u}^i_{k+1}(H) \\ \mathbf{u}^i_{k+1}(H/C) \\ \eta^i_{k+1}(H) \end{bmatrix} = \begin{bmatrix} \mathbf{u}^{\star,i}(H) \\ \mathbf{u}^{\star,i}(H/C) \\ -\mathbf{F}^{\text{int},i}_k(H) - \mathbf{K}(H,H)\cdot\mathbf{u}^i_k(H)\mathbf{K}(H,H/C)\cdot\mathbf{u}^i_k(H/C) \end{bmatrix} \tag{38}$$

After convergence, and once $\mathbf{u}^i(H)$, $\mathbf{u}^i(H/C)$ and $\eta^i(H)$ are obtained, nodal reaction forces exerted by the cell at cell-hydrogel boundary nodes are obtained as a postprocessing as $\mathbf{F}^{\text{ext},i}(H/C) = \mathbf{F}^{\text{int},i}(\mathbf{u}^i(H/C))$ according to Eqs. (36)–(38). Note that, in this case, the equilibrium of internal with external forces is prescribed, although these external forces are the unknown quantities in the modeling. However, since null external (body) forces are prescribed in the hydrogel interior domain in the overall formulation (38), the computation of cell forces is affected by this imposition, and hence they are more accurate than as computed without this constraint (as in the forward method). The efficiency of the proposed inverse method and the proof of this affirmation is shown in the results section.

The overall developed numerical method is summarized below.

Box 1: Solution algorithm of the developed PBNIM in TFM.

1. Obtain the displacement field vector $\mathbf{u}^\star$ by applying any of the displacement field recovery methods mentioned earlier (see section 2).
2. Build a finite element mesh of the imaged hydrogel region of interest around the embedded cell. Select hydrogel internal nodes and cell boundary nodes.
3. Interpolate the given displacement field at FE node locations $\rightarrow$ $\mathbf{u}^\star$.
4. Initialize $k = 0$, $\mathbf{u}_0 = \mathbf{0}$,
5. DO WHILE $||\mathbf{u}_{k+1} - \mathbf{u}_k||/||\mathbf{u}_{k+1}|| >$TOL
   - 5.1 FOR $e = 1..N_{el}$
     - i. Obtain element tangent stiffness matrices $\mathbf{K}^{(e)}$.
     - ii. Obtain element vector forces $\mathbf{F}^{(e),\text{int}}_k$.

   END FOR.

View Article Online
DOI: 10.1039/D0SM00789G

5.2 Assemble and obtain $\mathbf{K}$, $\mathbf{F}_k^{\text{int}}$.

5.3 Order $\mathbf{K}$ and $\mathbf{F}_k^{\text{int}}$ for cell boundary nodes H/C and hydrogel (internal) nodes H. Assemble the system (38) and solve.

END DO

6. Obtain converged solution $\mathbf{u}$.

7. Obtain remaining variables, i.e. stresses and tractions, for a given displacement field $\mathbf{u}$ as elaborated in section 3.

The numerical algorithm shown in box 1 was implemented using code programming in Matlab R2017a and Abaqus Simulia 6.14. Specifically, the main code implementation of box 1 was developed in Matlab. First, the input displacement field and the binary (voxelized) mask of the microscopy images are loaded. Then, the finite element mesh (point 2 in box 1) is built from the binary mask, using the tool Iso2Mesh of Matlab[39]. Then, the Abaqus input (inp) files are automatically written from the generated mesh and the loaded displacement field using a Matlab script. Abaqus is then externally called from Matlab in the main code file. Element tangent stiffness matrices and internal element vector forces (point 5.1 in box 1) are obtained as a request in the inp file. The assembly and solution of the system (38) is performed in Matlab following the scheme shown in box 1. Results are loaded in Matlab from Abaqus and visualized using the software GID.

The accuracy of the implemented method is analyzed by means of the error indicators defined in the next section for the example application introduced in section 7.

6 Analysis

The following mechanical variables are introduced for analysis purposes:

- *Displacement,* u^i *(*μm*)*: the magnitude of the displacement field vector at each FE node i.
- *Traction,* t_i *(Pa)*: the magnitude of the traction vector at each FE node i of the cell boundary.

To validate the proposed methods, the error recovering mean and extreme values of the mechanical variables in the cell surface region and in the hydrogel region was computed as described below. The purpose of assessing both the mean and extreme values of cell mechanical activity is because both can be relevant for the study of cell (mechanical) behaviour.

Let y_a^b represent a set of measures a of the mechanical variables at region b. Measures a refer to mean values m or extreme values e of the mechanical variables. Regions b refer to the cell boundary region c or hydrogel region h. Therefore, the following four sets are defined:

$$y_m^c = \{x^i\}, \quad i \in \text{cell boundary nodes} \tag{39}$$

$$y_m^h = \{x^i\}, \quad i \in \text{hydrogel nodes} \tag{40}$$

$$y_e^c = \{x^i \ : \ x^i > E[x^i] + k \cdot std[x^i]\}, \quad i \in \text{cell boundary nodes} \tag{41}$$

$$y_e^h = \{x^i \ : \ x^i > E[x^i] + k \cdot std[x^i]\}, \quad i \in \text{hydrogel nodes} \tag{42}$$

where $x^i = u^i, t_i^n, \sigma^i$ as defined above, $E[\bullet]$ and $std[\bullet]$ are the expectation and standard deviation of $\bullet$, respectively, and k defines the extreme level of the variable and is set to 1 in this paper. Moreover, the error of the quantities versus the ground truth solution (GT) is defined as follows:

$$z_a^b = 100 \cdot (1 - corr[y_a^b, y_a^b|_{GT}]), \tag{43}$$

where $corr[y_a^b, y_a^b|_{GT}]$ is the correlation coefficient between the probability density functions (PDF) of variable y_a^b and its corresponding ground truth (GT) solution. According to the definition in Eq. (43), the following error indicators are analyzed just by substition of corresponding variables y_a^b in Eq. (43):

- u_m^c: Error indicator of the displacement mean variable at the cell boundary region.
- u_m^h: Error indicator of the displacement mean variable at the hydrogel region.
- u_e^c: Error indicator of the displacement extreme variable at the cell boundary region.
- u_e^h: Error indicator of the displacement extreme variable at the hydrogel region.
- t_m^c: Error indicator of the traction mean variable at the cell boundary region.
- t_e^c: Error indicator of the traction extreme variable at the cell boundary region.

7 Examples of application

Human umbilical vein endothelial cells (HUVECs) were embedded in 1.2 mg/ml collagen type I hydrogels (a mixture of rat tail Collagen R, 2mg/ml and bovine skin Collagen G, 4mg/ml both from Matrix Bioscience) at low cell densities, so that they appeared as single, isolated cells. For more information about the critical parameters and troubleshoting for collagen gel preparation see previous published work[40,41]. HUVECs expressing Green Fluorescent Protein (GFP) were imaged by means of a Leica SP8 confocal microscope using a 25× NA 0.95 water-immersion objective, with a voxel size of $0.57 \times 0.57 \times 1\ \mu\text{m}^3$. Cells were imaged using 2-photon excitation at 404 nm and detection of its fluorescence emission with a 550/200 nm single-bandpass filter. A total of 5 typical HUVECs were selected and imaged. The image was enhanced by a contrast stretching operation and segmented by means of Otsu's thresholding, resulting in a 3D binarized image of a cell geometry.

View Article Online
DOI: 10.1039/D0SM00789G

Then, the voxelized cell boundary geometries were meshed using the Matlab tool Iso2Mesh[39]. The cell boundary geometry was centered in a box (matrix) with dimensions given in Table 1. The meshes of the hydrogel included tetrahedra with linear interpolation and corresponding nodes (see figs. 3, S1 and Table 1). The volume of the cell over the volume of the box ratio, as well as the mesh size parameters, were kept as constant for all the 5 cells in order to perform the numerical experiments under the same conditions. The hydrogel was assumed to be a hyperelastic Neo-Hookean material with an equivalent elastic modulus of 1645 Pa (in accordance with Steinwachs and co-workers[14] for the same collagen hydrogel composition) and 0.45 [–] for the Poisson's ratio.

Table 1 Hydrogel (box) dimensions and FE mesh data for each cell of the study.

Cell	Box size [μm^3]	FE mesh elements	FE mesh nodes
1	133× 133× 80	200820	37602
2	118× 118× 78	161622	30597
3	166× 166× 60	212904	40200
4	119× 119× 68	150814	28549
5	104× 104× 67	102539	19543

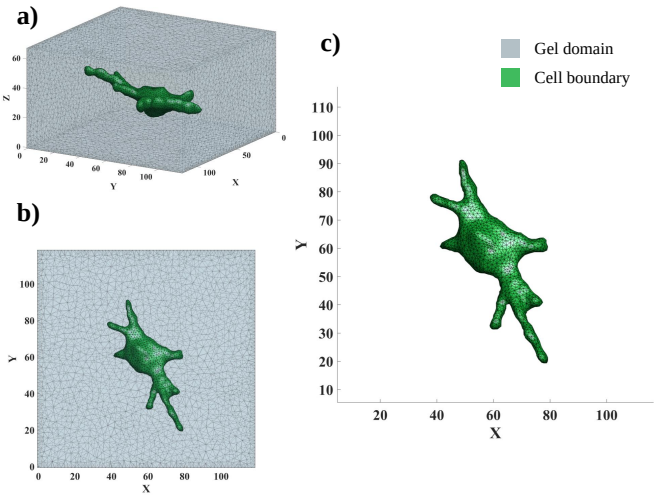

Fig. 3 FE mesh of a human umbilical vein endothelial cell (HUVEC) embedded in 1.2 mg/ml collagen type I hydrogel (cell #4 of a total of 5 cells, see fig. S1), used for TFM analysis. (a) 3D view and (b) top view of the cell (boundary) mesh. (c) Top view of the cell (boundary) mesh. Coordinates are in μm.

The ground truth solution of the problem was synthetically generated by applying a contractile force state in the cell's protrusions along the main protrusion direction (see figs. 4 and S2). First, the software program GID was used for manual selection of the nodes at the boundary of the cell protrusions. Then, nodal forces parallel to the protrusion axes were applied at these nodes. No force was applied at the rest of the nodes of the cell surface. Nodal force magnitude (per node) was constant for each cell, such that the order of magnitude of the resulting maximum displacements was similar to those shown in previous works[12]. The number of protrusions and magnitude of forces (per node) is detailed in Table 2 for each cell of the study. Nodal normal displacements on the hydrogel bounding box were set to zero in 3 orthonormal faces to avoid rigid body motions. The cell interior was modelled as a hole. The ground truth solution in terms of cell boundary tractions and displacements was obtained using Abaqus Simulia 6.14 software.

Table 2 Number of considered protrusions and magnitude of protrusive contractile forces (per node) for each cell of the study.

Cell	Protrusions	Force magnitude [pN]
1	2	395.78
2	4	487.46
3	2	341.53
4	6	448.22
5	4	668.90

Following the analogy with the TFM methodology (see introduction and section 2), the displacement field was recovered by mimicking bead-based displacement calculations. In this work, different bead densities expressed as percentage of beads per voxel were simulated, for each considered cell, using the following approach. The number of sampled voxels were calculated for each bead density case as:

$$n = \frac{bd}{100} \cdot \prod_{i=1}^{3} \frac{bs(i)}{vs(i)} \tag{44}$$

where bd is the bead density (in %), $bs(i)$ is the box size in dimension i and $vs(i)$ is the voxel size in dimension i (in μm). Four different bead densities were considered, namely, 0.5, 1, 5 and 10% (see Table 3). A wide bead density range was selected to cover both theoretical and experimental values presented in previous works[12,29,42–44].

Table 3 Bead densities used in this study. The corresponding concentrations, number of sampled points n, and inter-bead distance are included to ease the comparison with other works. (IBD: Inter-bead distance, defined as the average of the distances between one bead and its nearest neighbor). Parameters n and IBD were averaged over the 5 considered cells.

Bead density [%]	Concentration [beads/μ m^3]	n	IBD [μm]
0.5	0.02	17979	2.26
1	0.03	35960	1.78
5	0.15	179802	1.04
10	0.31	359604	0.82

Next, for each cell of study, the ground truth displacement values were evaluated at n random bead positions by means of linear interpolation of the nodal displacements (from the ground truth FEM simulation). Finally, a corrupted displacement field was obtained by interpolating the n displacement values from the previous step to the position of the FE nodes. In this work, this procedure is repeated 20 times (20 bead realizations) and then averaged, for each bead density case, in order to provide representative performance results. This corrupted (interpolated and averaged) displacement field is further referred to as the recovered displacement field used as input for the forward and inverse method, and at the same time is equal to the displacement field provided by the forward method (as the latter method treats the recovered displacement field as exact). As a validation of the

View Article Online
DOI: 10.1039/D0SM00789G

developed code, we checked that an error free (uncorrupted) displacement field solution, used as input in the forward and inverse solvers, converges exactly to the same solution both for the forward and proposed inverse methods. The converged solution was in fact equal to the ground truth solution, as expected.

Fig. 4 Prescribed uniform nodal forces (see magnitude in Table 2) synthetically applied along 6 selected protrusions of cell #4. Scale bar 20 μm.

8 Results

Results are given for the solutions provided by both the PBNIM and forward methodologies for the different considered bead densities and compared to the ground truth solution. In this section, graphical results are shown for cell #4 for illustrative purposes, while the rest of analyzed results of the different cells is available in the supplementary information (SI) section. However, the analysis and discussion in this section considers all 5 analyzed cells.

Figs. (5) and (6) show the displacement magnitude on the cell #4 boundary and in the mid cross section of the hydrogel, respectively. Qualitatively, minimal differences are found between the inverse and forward methodologies for a given bead density. This behavior is also seen for the other 4 cells (see figs. S3-S10). As expected, both the inverse and forward solutions approach the ground truth solution with increasing (sampling) bead density. It is important to remark that the forward displacement field solution is the result of a downsampling and interpolation procedure from the voxel imaged position of the beads to the finite element mesh. The improvement of the forward displacement field with increasing bead density is therefore due to the increase of the dimension of the interpolation dataset. On the other hand, the inverse displacement field is dependent both on the recovered displacements, but also on the optimisation procedure shown in box 1.

Solutions for traction magnitude are depicted in fig. (7) on the cell #4 boundary. In this case, qualitative differences are found between the inverse and forward solutions versus the ground truth one. Again, this finding is reproduced in other analyzed cells (see figs. S11-S14). The inverse method leads to traction distributions that are qualitatively more similar to the ground truth solution for the considered range of bead densities. Both the inverse and forward solutions improve with increasing bead density in comparison to the ground truth solution. The improvement is more evident for the forward method, which implies that the proposed inverse method is less sensitive to bead density (sampling), and which is corroborated by fig. (8). This behavior is further explained below.

The different error indicators, as defined in section 6 (Eq. (43)), are presented in fig. (8), which quantify the performance of the inverse and forward approaches for the different considered bead densities. Overall, displacement-based error indicators (fig. 8b,d,e) show similar trends and values for both methods and for the entire range of bead densities, with the inverse method generally performing slightly better (lower error indicator averaged over the 5 cells). However, results show significant differences and improved performance of the inverse method in displacement-based error indicators (averaged over the 5 cells, fig. 8b,d,e) at low bead densities, showing large differences for extreme displacement-based error indicator (fig. 8d,e). As an exception, the mean displacement-based error indicator in the hydrogel region (fig. 8a) shows a slightly better performance in the forward method, although both the forward and inverse methods provide negligible errors. It is worth remarking that the computed displacement field is conditioned both by an interpolation procedure from beads to interior hydrogel nodes, and by an extrapolation procedure from beads to cell boundary nodes (the latter due to a lack of positional information at the cell interface). The values of the displacement-based error indicators were substantially lower in the hydrogel region (fig 8 a,d) than at the cell boundary (fig 8 b,e) for all bead densities. This suggests that the extrapolation procedure inherently leads to higher errors than interpolation.

In contrast, tractions are recovered much more accurately by means of the inverse method, compared to the forward method. Mean traction-based error indicators (as averaged over the 5 cells) reach much higher values (between 53% and 30% for low to high bead densities) in case of the forward method, while for the inverse method this error indicator ranges from 17% to 8% for low to high bead densities (fig. 8c). Also, for the recovery of extreme traction values, the inverse method outperforms the forward method, with the value of the corresponding error indicator ranging from 26% to 7% for the forward method, and from 7% to 5% for the inverse method, for low to high bead densities (fig. 8f).

Traction-based error indicators are relatively insensitive to bead density in the case of the inverse method. Combined with the fact that for the inverse method, errors for traction recovery are already at low values for the lowest bead density, it suggests that the use of relatively low bead densities in TFM experiments could be acceptable when tractions are recovered by means of the inverse method. This effect is explained by the fact that in the case of the forward method recovered tractions at the cell boundary are strongly dependent on the extrapolation procedure referred to previously, and hence to the presence of beads close to

View Article Online
DOI: 10.1039/D0SM00789G

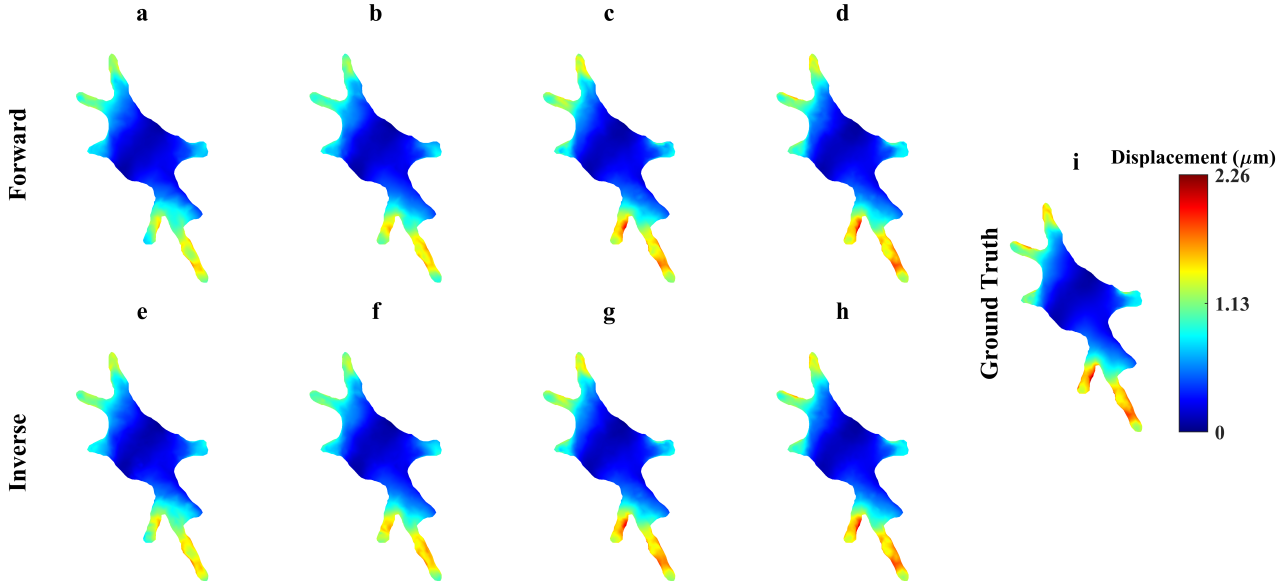

Fig. 5 Displacement magnitude [μm] on cell #4 boundary (top view). Forward method, for a bead density of: (a) 0.5%, (b) 1%, (c) 5% and (d) 10%. Inverse method, for a bead density of: (e) 0.5%, (f) 1%, (g) 5% and (h) 10%. (i) Ground truth results.

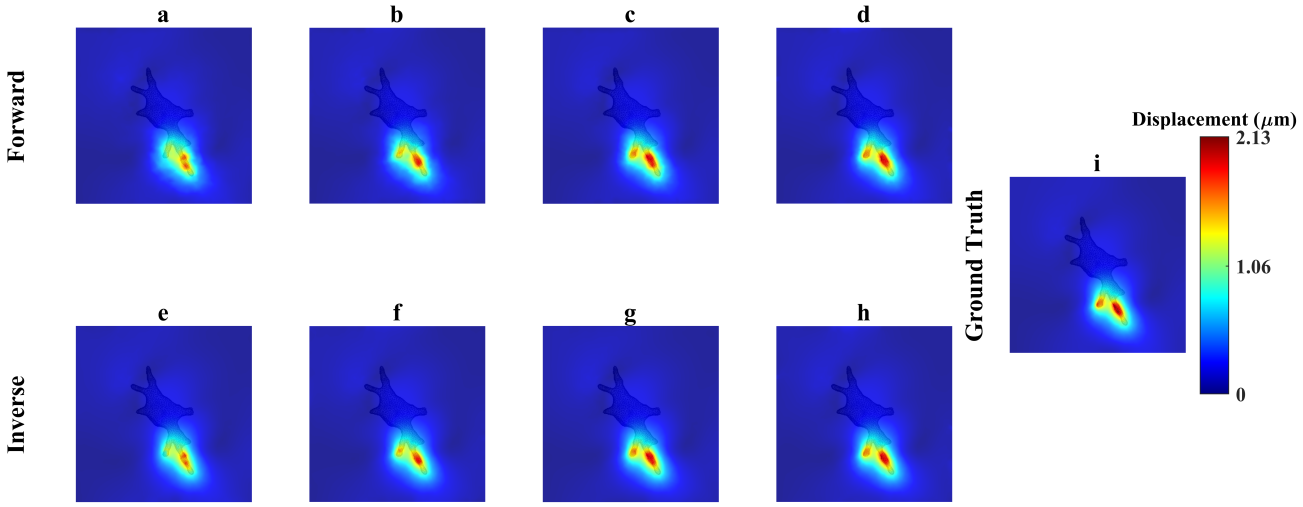

Fig. 6 Displacement magnitude [μm] on cell #4 boundary and mid cross section of the hydrogel (3D view). Forward method, for a bead density of: (a) 0.5%, (b) 1%, (c) 5% and (d) 10%. Inverse method, for a bead density of: (e) 0.5%, (f) 1%, (g) 5% and (h) 10%. (i) Ground truth results.

View Article Online
DOI: 10.1039/D0SM00789G

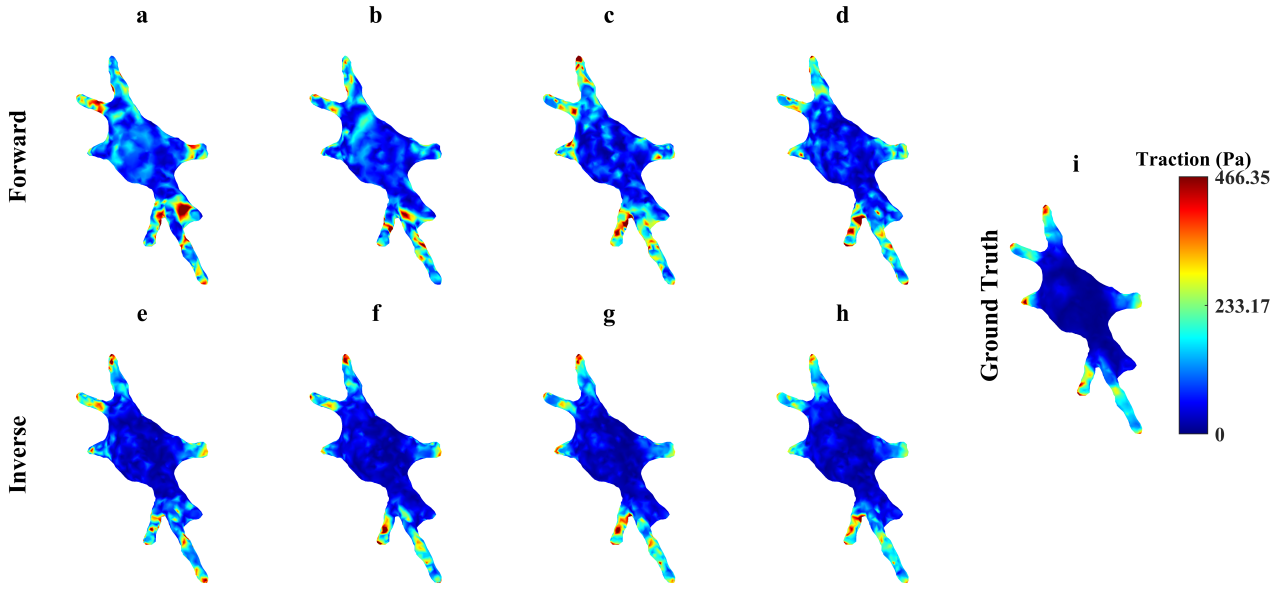

Fig. 7 Traction magnitude [*Pa*] on cell boundary #4 (top view). Forward method, for a bead density of: (a) 0.5%, (b) 1%, (c) 5% and (d) 10%. Inverse method, for a bead density of: (e) 0.5%, (f) 1%, (g) 5% and (h) 10%. (i) Ground truth results.

the boundary (which statistically improves with increasing number of sampling beads). Specifically, inter-bead distance (on average) varies in the range of 0.82–2.26 μm for a bead density of 0.5-10% (table 3). Tractions recovered by the inverse method are also a function of the imposition of the equilibrium condition which is independent of the number of beads.

The average value of the different error indicators (averaged over the considered bead densities and cells) is plotted in fig. 9, for both the inverse and forward method. Except for the case of mean displacement errors (which values are negligible both for the inverse and forward methods), this figure corroborates that the inverse method outperforms the forward method for all the defined error indicators, especially tractions (variable of interest in TFM). Together with the results of figs. 7 (and corresponding figs. S11-S14 for the other 4 analyzed cells), it suggests that the accuracy of cell traction recovery is improved by the imposition of the equilibrium constraint in the hydrogel region, as provided by the inverse method.

9 Conclusions

A new inverse method for cell traction recovery in the context of 3D nonlinear elasticity was proposed in this paper. Both the theoretical background and the numerical implementation were elaborated in detail. The method minimises the difference between a measured and calculated displacement field in the hydrogel region surrounding the cell, and imposes a physical constraint to possible displacement field solutions, namely equilibrium of forces in the hydrogel region. The equilibrium constraint equation was formulated using the Principle of Virtual Work and discretised by means of the Finite Element Method in the context of finite strain nonlinear elasticity. Enhanced accuracy for traction and displacement recovery with respect to the forward method was shown for a total of 5 real cell geometries embedded in a hydrogel that was modelled by means of a hyperelastic, quasi-incompressible Neo Hookean constitutive model, as a first approach without loss of generality. While this material model is unlikely to capture the full nonlinear elastic response of collagen hydrogels (as used here for embedding HUVEC cells and acquiring their geometry), we applied this material model for reasons of simplicity. This simplification should not affect the general conclusions of this study concerning the merits of the new inverse method, especially since its implementation is compatible with any nonlinear elastic material model. Moreover, hydrogel materials undergo a viscoelastic response as evidenced in the literature[45,46]. The general theoretical framework shown in the present paper is also valid to extend to the viscoelasticity case. In particular, the constitutive model (Eq. (11)) needs to be reformulated, and then numerically implemented following for instance a convolution representation for the viscoelastic behavior. Classical numerical approaches can be followed for the extension of the nonlinear approach to account for viscoelasticity[47].

The deviation between the recovered displacement field (which is equal to the displacement field of the forward solution) and the ground truth displacement field is low on average. On the contrary, the deviation between the recovered tractions and the ground truth tractions is more than 3 times for mean traction-based error indicator according to fig. 8c, depending on the cell of interest, with faster convergence as a function of bead density (i.e. deviations that are already low for relatively low bead densities and that are less sensitive to a further increase in bead density) for the inverse method. The cases where little improvement in tractions is found with bead density, could be attributed to unavoidable extrapolation errors in the displacement field due to lack of positional information at the cell boundary,

View Article Online
DOI: 10.1039/D0SM00789G

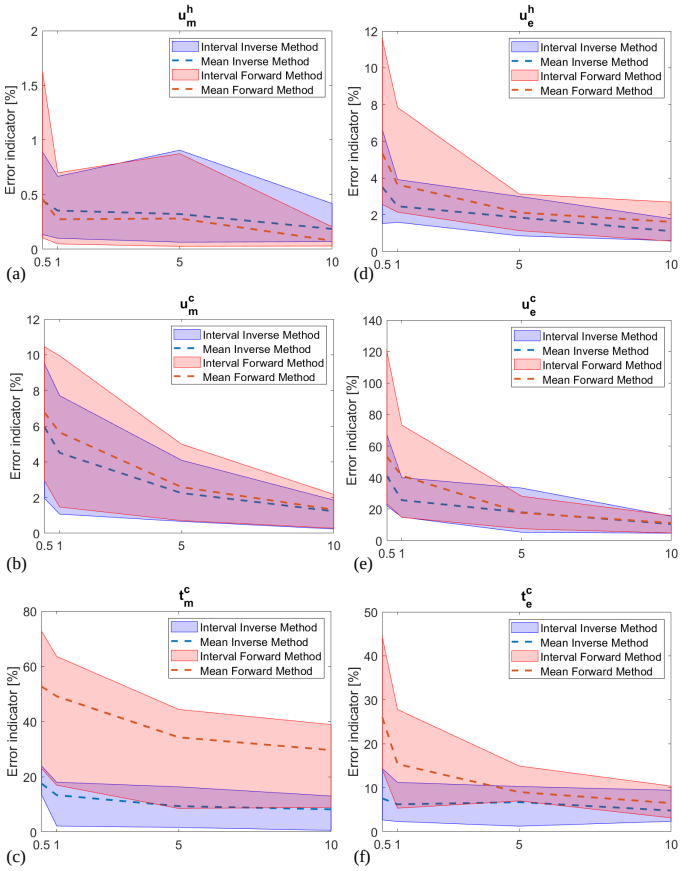

Fig. 8 Error indicators as a function of bead density. Mean value error indicators for (a) displacements in hydrogel region u_m^h, (b) displacements at cell boundary u_m^c, and (c) tractions at cell boundary t_m^c. Extreme value error indicators for (d) displacements in hydrogel region u_e^h, (e) displacements at cell boundary u_e^c, and (f) tractions at cell boundary t_e^c. The intervals represent the range of variation of values for the 5 analyzed cells (see SI section). Dashed lines represent the average of values over the 5 analyzed cells.

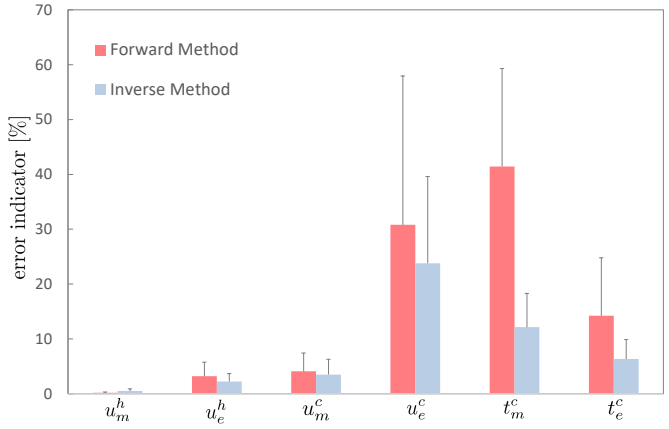

Fig. 9 Average and standard deviation of error indicators, averaged over the considered bead density values and the 5 analyzed cells.

which highlights the importance of a proper sampling procedure. Note that this behavior cannot be interpreted strictly as an asymptote for the considered range of bead densities. These errors are likely to decay to negligible values for extremely large bead densities. Nonetheless, remark that bead densities higher than the analyzed ones are not feasible in practice, because conventional (diffraction-limited) optical microscopy would not be able to resolve the individual beads due to overlapping point spread functions, which hampers the tracking of bead movements[48]. Moreover, the use of higher bead densities could change the mechanical properties of the hydrogel as well. In addition, only errors related to interpolation/extrapolation from bead to nodes were considered. Even though this is an important source of error in TFM, consideration of additional sources of error (e.g. related to the microscope setup) may yield an additional improvement of the inverse versus the forward method.

While this study focuses on the establishment of a new inverse method that preserves mechanical equilibrium and its comparison to a forward method, future efforts should aim at comparing different inverse methods, by applying them to a number of realistic, synthetically generated data sets that could serve as benchmarking problems for the assessment of TFM accuracy. For example, it would be interesting to compare our inverse method to an inverse method that employs Tikhonov regularization, the latter having the disadvantage that it does not ensure the fulfilment of mechanical equilibrium in the hydrogel.

In conclusion, the evaluation of the performance of the inverse method presented in this paper suggests that this framework may be used to accurately estimate cell displacements and tractions in 3D TFM experiments with nonlinear elastic hydrogels, even for relatively low bead densities that are compatible with TFM experimental procedures.

Conflicts of interest

There are no conflicts to declare.

Acknowledgements

J.A.S.–H. was supported by the José Castillejo fellowship of the Ministerio de Educación, Cultura y Deporte of Spain, grant number CAS17/00096, and Spanish Ministry of Economy and Competitiveness (MINECO) through the project PGC2018-097257-B-C31. J.B.–F. and H.V.O were supported by KU Leuven internal funding C14/17/111. J.B.–F. was supported by the Research Foundation Flanders (FWO) (travel grant for a long stay abroad to J.B.–F, FWO grant V413019N). M.C. was supported by the FWO grant 12ZR120N. The financial support is gratefully acknowledged.

Notes and references

1 D. Ingber, *Annals Med.*, 2003, **38**, 546–577.
2 D. E. Discher, P. Janmey and Y. L. Wang, *Science*, 2005, **310**, 1139–1143.
3 A. J. Engler, S. Sen, H. L. Sweeney and D. E. Discher, *Cell*, 2006, **126**, 677–689.
4 C. S. Chen, *J. Cell Sci.*, 2008, **121**, 3285–3292.

View Article Online
DOI: 10.1039/D0SM00789G

5 D. A. Fletcher and R. D. Mullins, *Nature*, 2010, **463**, 485–492.

6 C. M. Denais, R. M. Gilbert, P. Isermann, A. L. McGregor, M. Lindert, B. Weigelin, P. M. Davidson, P. Friedl, K. Wolf and J. Lammerding, *Science*, 2016, **352**, 353–358.

7 M. Dembo, T. Oliver, A. Ishihara and K. Jacobson, *Biophys. J.*, 1996, **70**, 2008–2022.

8 M. Dembo and Y. L. Wang, *Biophys. J.*, 1999, **76**, 2370–2316.

9 J. P. Butler, I. M. Tolic-Norrelykke, B. Fabry and J. J. Fredberg, *Am. J. Physiol. Cell Physiol.*, 2002, **282**, C595–C605.

10 J. C. D. Alamo, R. Meili, B. Alonso-Latorre, J. Rodriguez-Rodriguez, A. Aliseda, R. A. Firtel and J. C. Lasheras, *Proc. Natl. Acad. Sci.*, 2007, **104**, 13343–13348.

11 W. R. Legant, C. K. Choi, J. S. Miller, L. Shao, L. Gao, E. Betzig and C. S. Chen, *Proc. Natl. Acad. Sci. USA*, 2013, **110**, 881–886.

12 W. R. Legant, J. S. Miller, B. L. Blakely, D. M. Cohen, G. M. Genin and C. S. Chen, *Nat. Methods*, 2010, **7**, 969–971.

13 J. Toyjanova, E. Bar-Kochba, C. López-Fagundo, J. Reichner, D. Hoffman-Kim and C. Franck, *PLOS ONE*, 2014, **9**, e90976.

14 J. Steinwachs, C. Metzner, K. Skodzek, N. Lang, I. Thievessen, C. Mark, S. Muenster, K. E. Aifantis and B. Fabry, *Nat. Methods*, 2016, **13**, 171–176.

15 Y. Du, S. C. B. Herath, Q. G. Wang, H. H. Asada and P. C. Y. Chen, *Acta Biomater.*, 2018, **67**, 215–228.

16 H. Farid and E. P. Simoncelli, *IEEE Trans. Image Process*, 2004, **13**, 496–508.

17 E. Bar-Kochba, J. Toyjanova, E. Andrews, K.-S. Kim and C. Franck, *Exp. Mech.*, 2015, **55**, 261–274.

18 Z. Yang, J. S. Lin, J. Chen and J. H. C. Wang, *J. Theor. Biol.*, 2006, **242**, 607–616.

19 S. S. Hur, Y. Zhao, Y. S. Li, E. Botvinick and S. Chien, *Cell. Mol. Bioeng.*, 2009, **2**, 425–436.

20 U. S. Schwarz and J. R. D. Soine, *Biochim. Biophys. Acta.*, 2015, **1853**, 3095–3104.

21 S. V. Plotnikov, B. Sabass, U. S. Schwarz and C. M. Waterman, *High resolution traction force microscopy*, 2014.

22 P. C. Hansen, *Rank-deficient and discrete ill-posed problems: Numerical aspects of linear inversion*, 1998.

23 D. Ambrosi, *SIAM J. Appl. Math.*, 2006, **66**, 2049–2060.

24 D. Ambrosi, A. Duperray, V. Peschetola and C. Verdier, *J. Math. Biol.*, 2009, **58**, 163–181.

25 G. Vitale, L. Preziosi and D. Ambrosi, *Inverse Problems*, 2012, **28**, 095013.

26 M. Kirchdoerfer and M. Ortiz, *Comput. Methods Appl. Mech. Engrg.*, 2017, **326**, 622–641.

27 M. R. K. Mofrad, H. Karcher and R. D. Kamm, *Continuum elastic or viscoelastic models for the cell*, Cambridge University Press, 2006.

28 I. M. Tolić-Nørrelykke, J. P. Butler, J. Chen and N. Wang, *Amer. J. Physiol.-Cell Physiol.*, 2002, **4**, C1254–C1266.

29 Y. Du, S. C. B. Herath, Q. Wang, D. Wang, H. H. Asada and P. C. Y. Chen, *Sci. Reports*, 2016, **6**, 21,362.

30 S. J. Han, Y. Oak, A. Groisman and G. Danuser, *Nature Meth.*, 2015, **12**, 653–656.

31 A. Jorge-Penas, A. Izquierdo-Alvarez, R. Aguilar-Cuenca, M. Vicente-Manzanares, J. M. Garcia-Aznar, H. V. Oosterwyck, E. M. De-Juan-Pardo, C. Ortiz-De-Solorzano and A. Munoz-Barrutia, *PLoS ONE*, 2015, **10**, 1–22.

32 P. Moreo, J. M. Garcia-Aznar and M. Doblare, *Acta Biomater.*, 2008, **4**, 613–621.

33 J. A. Sanz-Herrera, P. Moreo, J. M. Garcia-Aznar and M. Doblare, *Biomaterials*, 2009, **30**, 6674–6686.

34 G. A. Holzapfel, *Nonlinear solid mechanics. A continuum approach for engineering*, John Wiley & Sons, England, UK, 2000.

35 D. Rueckert, L. I. Sonoda, C. Hayes, D. L. G. Hill, M. O. Leach and D. J. Hawkes, *IEEE Trans. Med. Imagng.*, 1999, **18**, 712–721.

36 O. C. Zienkiewicz and R. L. Taylor, *The Finite Element Method*, Butterworth–Heinemann, Oxford, 5th edn, 2000.

37 J. Bonet and R. D. Wood, *Nonlinear continuum mechanics for finite element analysis*, Cambridge University Press, Cambridge, 1997.

38 M. A. Crisfield, *Non-linear finite element analysis of solids and structures*, John Wiley & Sons, England, UK, 1991.

39 Q. Fang and D. Boas, *Proc. IEEE Int. Symp. Biomed. Imagng.*, 2009, 1142–1145.

40 M. Cóndor, J. Steinwachs, C. Mark, J. García-Aznar and B. Fabry, *Curr. Protoc. Cell Biol.*, 2017, **75**, 10.22.1–10.22.20.

41 M. Cóndor, C. Mark, R. Gerum, N. Grummel, A. Bauer, J. García-Aznar and B. Fabry, *Biophys. J.*, 2019, **116**, 1305–1312.

42 C. Franck, S. A. Maskarinec, D. A. Tirrell and G. Ravichandran, *PLoS ONE*, 2011, **6**,.

43 C. N. Holenstein, U. Silvan and J. G. Snedeker, *Sci. Rep.*, 2017, **7**, 41633.

44 C. N. Holenstein, C. R. Lendi, N. Wili and J. G. Snedeker, *Comput. Meth. Biomech. Biomed. Eng.*, 2019, 1–8.

45 G. W. Brodland, V. Conte, P. G. Cranston, J. Veldhuis, S. Narasimhan, M. S. Hutson, A. Jacinto, F. Ulrich, B. Baum and M. Miodownik, *Proc. Natl. Acad. Sci. U.S.A.*, 2010, **107**, 22111–22116.

46 L. Casares, R. Vincent, D. Zalvidea, N. Campillo, D. Navajas, M. Arroyo and X. Trepat, *Nat. Mater.*, 2015, **14**, 343–351.

47 J. C. Simo and T. J. R. Hughes, *Computational Inelasticity*, Springer, 1998.

48 H. Colin-York and M. Fritzsche, *Curr. Opin. Biomed. Eng.*, 2018, **5**, 1–5.